Nuclear Instruments and Methods in Physics Research A 729 (2013) 316–321

Contents lists available at ScienceDirect

Nuclear Instruments and Methods in Physics Research A

journal homepage: www.elsevier.com/locate/nima

Improving quantitative neutron radiography through image restoration

D.S. Hussey [a,*], K.J. Coakley [b], E. Baltic [a], D.L. Jacobson [a]

[a] National Institute of Standards and Technology, Gaithersburg, MD 20899, USA
[b] National Institute of Standards and Technology, Boulder, CO 80305, USA

ARTICLE INFO

Article history:
Received 18 June 2013
Received in revised form
1 July 2013
Accepted 2 July 2013
Available online 20 July 2013

Keywords:
Image restoration
Neutron imaging
Point spread function

ABSTRACT

Commonly in neutron image experiments, the interpretation of the point spread function (PSF) is limited to describing the achievable spatial resolution in an image. In this article it is shown that for various PSF models, the resulting blurring due to the PSF affects the quantification of the neutron transmission of an object and that the effect is separate from the scattered neutron field from the sample. The effect is observed in several neutron imaging detector configurations using different neutron scintillators and light sensors. In the context of estimation of optical densities with an algorithm that assumes a parallel beam, the effect of blurring fractionates the neutron signal spatially and introduces an effective background that scales with the area of the detector illuminated by neutrons. Examples are provided that demonstrate that the illuminated field of view can alter the observed neutron transmission for nearly purely absorbing objects. It is found that by accurately modeling the PSF, image restoration methods can yield more accurate estimates of the neutron attenuation by an object.

Published by Elsevier B.V.

1. Introduction

Neutron radiography is a powerful non-destructive evaluation tool, enabling the visualization of two-phase flow phenomena in metallic matrices such as fuel cells and heat pipes. The strong interaction between neutrons and water enables measurements of small water volumes in these devices with a measurement sensitivity less than 100 pL possible (water thicknesses uncertainty less than 1 μm) [1]. This sensitivity is based only on counting statistics achievable at most neutron sources, and does not account for systematic uncertainties. Some sources of common systematic uncertainties encountered in measuring the water thickness in fuel cells include beam hardening, the residual water in the membrane during the dry image, bias due to low counting statistics, blurring due to finite spatial resolution that is quantified by a point spread function (PSF) [2], and a scattered neutron field from the sample [3]. In defining the image spatial resolution, the convention in neutron radiography is to determine the frequency at which the modulation transfer function (the Fourier transform of the PSF) reaches 10% of its maximum value. The discussion of the effects of the PSF has been primarily limited to the ability to resolve finer features in an image, for instance, better determination of the shape of the through-plane water content in an operating fuel cell [4]. However, there is another aspect of the PSF that has seen only minor attention in the neutron imaging community: in estimating the attenuation of an object, the tail of PSF can give rise to an effective additive background, the strength of which will vary with the size of the field of view and is such that one will underestimate the true neutron attenuation.

As demonstrated by Kramer et al. [5], the effect of the PSF is that one will observe less attenuation in regions of the object that have low neutron transmission due to the diffuse light from regions of the image with higher neutron transmission. If the PSF does not decay rapidly then all points of the detector medium that are illuminated by neutrons contribute to this background. Examples of slowly decaying PSF models include a Lorentzian and Voigt profile, whereas a Gaussian PSF has a rapid decay. Since neutron radiography relies on comparing two images, it is critical that this additive background be properly accounted for in the images of the reference state and of the object in order to obtain accurate estimates of the neutron attenuation. Accounting for the background due to the PSF requires deblurring the measured image (including the flatfield) through an image restoration algorithm. As shown in Kramer et al. [5], image restoration yields better estimates for the water thickness, especially in areas of the fuel cell with high water thickness (i.e. flooded channels). However, the restoration method used by Kramer et al. determined the PSF from a sub-image corresponding to $\sim 10^{-4}$ of the imaging area. While the image restoration was able to capture short range effects, the use of a sub-image precludes observing effects if the PSF has a long tail. The success of an image restoration is in large part determined by how accurate the functional representation of the PSF

* Corresponding author. Tel.:+1 301 975 6465.
E-mail address: daniel.hussey@nist.gov (D.S. Hussey).

0168-9002/$ - see front matter Published by Elsevier B.V.
http://dx.doi.org/10.1016/j.nima.2013.07.013

models the physical measurement system [6]. The reason for this is demonstrated in Fig. 1, in which the simulated neutron image of a completely absorbing disk for three different point spread functions is shown. In Fig. 1, the Gaussian model and the Lorentzian model characterized by the half-width, half maximum of 13 μm yield the same spatial resolution as defined by the point at which the modulation transfer function reaches 10% of its maximum value. As can be seen, with a Gaussian PSF, one would predict that the image of the disk will have little to no influence from the illuminated field of view since the intensity in the area under the disk is close to the floating point precision of the simulation, whereas a system with a Lorentzian PSF will have a larger background due to the illuminated field of view.

In this work, we assume a simple linear model for image formation where image degradation is due only to the imaging detector. In this model we do not include beam hardening and approximate the neutron beam as a parallel beam without beam divergence. The parallel beam approximation is valid for the experiments below since the geometric unsharpness was about 80 μm which is about three times smaller than the spatial resolution of the detector and this allows one to ignore beam divergence in determining and modeling the detector PSF. Similar to other imaging modalities, we model the measured neutron image in terms of a convolution of an unobserved integrated fluence image f and a discrete representation of the PSF. That is, we model the observed (e.g. grey levels or estimated number of neutrons) value for the pixel centered on location (x_i, y_j) as:

$$h(x_i,y_j) = \epsilon\sum_{k,l} f(x_k,y_l)\, g(x_i-x_k, y_j-y_l) + n(x_i,y_j), \quad (1)$$

where $f(x_k, y_l)$ is the unobserved integrated fluence for the pixel centered on location (x_k, y_l); ϵ is a detector efficiency factor; g is a discrete point spread function; and $n(x,y)$ is the noise in the system, due to readout electronics, Poisson counting statistics, etc. In this model, the true image f is the neutron transmission where the incident fluence I_0 is attenuated by the total neutron scattering cross-section Σ of the object:

$$f(x_i,y_j) = I_0(x_i,y_j)\exp\left(-\int_0^z \Sigma(x_i,y_j,z)dz\right).$$

In the spatial frequency domain, after applying a Fourier transformation:

$$H(u,v) = \epsilon F(u,v)\, G(u,v) + N(u,v), \quad (2)$$

where G is the modulation transfer function. It should be pointed out that this formalism is for linear, translation invariant systems.

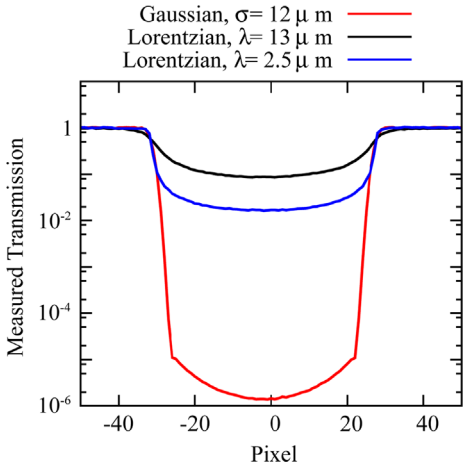

Fig. 1. Line scan of simulated neutron transmission through a completely attenuating disc of diameter 300 μm for three different PSF models. The detector was assumed to have a pixel pitch of 5 μm, and a full field of view of 300 pixels by 300 pixels. The Gaussian model is very insensitive to long range effects due to the rapid decay of the Gaussian.

In the case of a neutron detector based on a lens-coupled charge-coupled-device (CCD), this might not be the case, as the mirror and light-tight enclosure may produce scattered light, which will not necessarily be translation invariant. Further, if the detector has spatially varying gain or light sensitivity, the image formation described by Eqs. (1) and (2) is not strictly correct. If there are significant variations in the sensitivity, one would need to correct the raw data for this variation. Here we consider gain variations that are small (few percent) and approximate the gain as a constant in the detector. There are two consequences of Eq. (1): first, small image features such as edges are degraded (blurred) and second, each detector pixel contains an effective additive background that is dependent on the relative luminance of all other pixels. To demonstrate this, we model the discrete image data (in the absence of noise) as

$$\langle h(i,j)\rangle = \sum_{k,l} f(k\times l)g(i-k,j-l) = f(i,j)g(0,0) + b(i,j) \quad (3)$$

where

$$b(i,j) = \sum_{k,l} f(k\times l)\, g(i-k,j-l) - f(k\times l)\, g(0,0). \quad (4)$$

The size of b depends both on the area of the detector illuminated by neutrons and the decay of g. It should be emphasized that b is not a true background that is independent of the signal f, but rather strongly correlated with f through the detector blurring. As shown in Fig. 1, if g is modeled as a Gaussian, one would expect that the additive background would be negligibly small and insensitive to the illuminated area due to the rapid decay of the Gaussian. However, if g has a slower decay, as in the case of a Lorentzian distribution or a Voigt profile, the additive background can be large. It should be emphasized that one must consider the entire area of the detector illuminated by neutrons, and not just the field of view of the light sensor, as light from all portions of the scintillator may reach the sensor. An example of this background is shown in Fig. 2. A charge-coupled device (CCD) camera viewed a 300 μm thick, 30 cm × 30 cm NDg scintillator screen from Applied Scintillator Technologies[1] through a Nikon 50 mm lens. Shown in Fig. 2a is the image of the flat field (cropped to the main beam), which is shown at the same contrast level as the image of an aperture (Fig. 2b). A line profile (Fig. 2c) through the center portion of the aperture demonstrates that the flat field has a ~15% higher intensity than the aperture. Further, since the intensity in the open portion of the aperture is flat, the reduced intensity is not a result of insufficient spatial resolution but is rather due to the larger additive background in the flatfield.

2. Experimental

All subsequent images presented in this work were acquired at the BT2 neutron imaging facility, using a neutron beam with an L/D ratio of 600 corresponding to a fluence rate of about 5×10^6 cm^{-2} s^{-1}. The neutron imaging detector employed to acquire the images in this article was a Varian Paxscan 2520, high energy amorphous silicon (α-Si) flat panel detector with a field of view of 25 cm by 20 cm, and pixel pitch of 127 μm with active air cooling inside the housing. We focus on the amorphous silicon detector as it is the most used and best characterized detector at the NIST neutron imaging facility. The scintillator is composed of ZnS doped with [6] LiF and is 300 μm thick. All images were

[1] Certain trade names and company products are mentioned in the text or identified in an illustration in order to adequately specify the experimental procedure and equipment used. In no case does such identification imply recommendation or endorsement by the National Institute of Standards and Technology, nor does it imply that the products are necessarily the best available for the purpose.

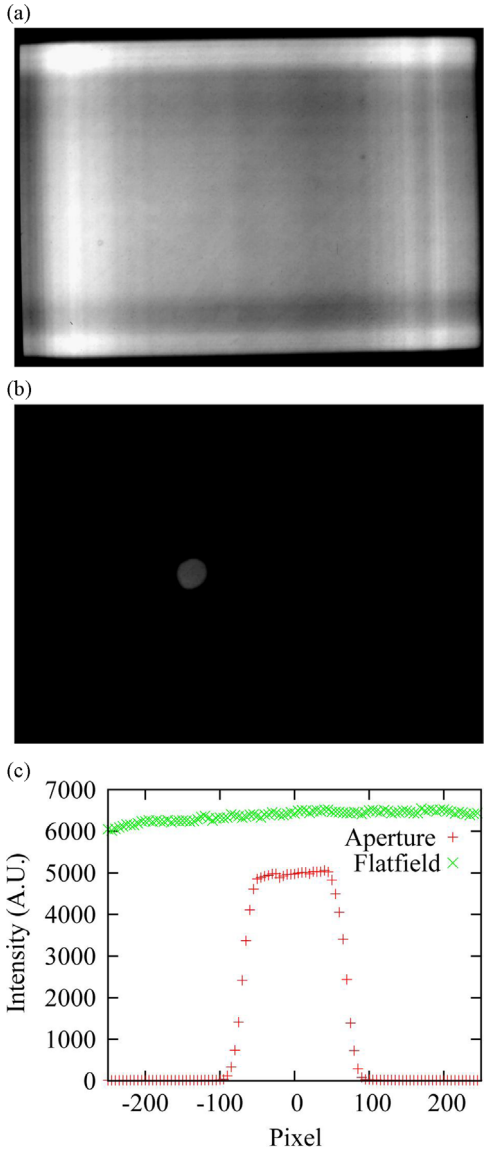

Fig. 2. Effective additive background observed with a scintillator and CCD system, flatfield (a), image of the aperture (b), and line scan through the aperture region (c).

acquired at a frame rate of 1 Hz for 30 min. In the detector hardware, the dark image is subtracted from the acquired image; dark images from before and after neutron exposure were compared to ensure that there was no drift between measurements. While the remainder of this article focuses solely on images acquired from the amorphous silicon detector, the effect of the illuminated field of view has been observed in CCD systems with 300 μm thick ZnS:LiF scintillators (Fig. 2) and Gadoxysulfide scintillators.

There have been previous reports about the effects of neutron scattering from a sample (primarily water) resulting in an additive background [3]. The scattered neutron field also has a slow decay going as $\cos(\theta)/(z^2+r^2)$, where r is the distance in the detector plane from the scattering center, z is the separation along the beam path between the scattering center and the detector, and θ is the angle between the neutron ray and the detector surface normal. We do not consider neutron scattering in this article as we focus only on the point spread function of the detector system. We do this in the examples provided below by isolating the effect of the illuminated field of view from a scattered neutron field by analyzing pure absorbing samples, analyzing samples with small total scattering cross-sections, and/or comparing images of the same sample acquired with both a masked and full field of view such that the contribution of the scattered neutron field is the same for all pixels in the image.

3. Results and analysis

Typically, the PSF of a neutron imaging detector is measured from the image of a sharp edge, which often can be fit equally by several PSF models due in part to counting statistics and restricting the field of view to the neighborhood of the edge [7]. Ideally, one would acquire a series of images of pinholes with decreasing diameter. Since the decay of the PSF is the goal of this article, the tail of the PSF will be more visible over the background if a large diameter pinhole is imaged. To determine the PSF for the α-Si detector, 1 mm thick Cd sheet with a 5 cm diameter hole was imaged both in the center and the edge of the field of view. Images with a 1 mm thick Cd sheet that fully covered the field view were used to measure the background contributions from electronic read-noise, dark current, gamma-rays, and epithermal and fast neutrons. For the case of the amorphous silicon detector used at the NIST neutron imaging facility, g was empirically determined by comparing the measured image of a Cd sheet with a 5 cm diameter hole to that of a model image. While a smaller diameter hole would better approximate a "point", the 5 cm was chosen so as to have a higher intensity to study the long tail of the PSF. The background was measured by placing the same thickness of Cd in front of the entire detector surface. The observed data was compared to a predicted image by convolving a trial PSF with the image of a sharp hole where the flatfield, deconvolved by the trial function, was used to generate the intensity at points inside the open region of the hole. The observed point spread function was very well approximated with a model that predicts a PSF that is symmetric in the horizontal and vertical directions of the following form:

$$g_{\alpha-\mathrm{Si}}(r) = A \times \left(1 - \frac{r}{\sqrt{l^2+r^2}}\right) \times \theta(L_x - |x|) \times \theta(L_y - |y|) \tag{5}$$

where A is a normalization constant, $r^2 = x^2 + y^2$, $\theta()$ is the Heaviside function, $L_{x,y}$ is half the image size in x or y, and $l = 11.157$ μm; l was varied on a grid until the difference between the measured and predicted images were minimized; changing l by $+/-0.002$ about 11.157 in a strongly deteriorated fit. A vertical line scan through the center of the hole in the observed and simulated data is shown in Fig. 3. For $r^2 \gg l^2$, $g_{\alpha\text{-Si}}$ has a similar decay as a Lorentzian. It should be emphasized that Eq. (5) is one model of the observed PSF and there may be a better functional form that better represents g.

In order to avoid a discussion of optimal restoration algorithms, we focus below only on neutron image data with very high signal to noise ratios (SNRs); as shown in Fig. 4, $|H(u,v)|/|N(u,v)| > 10$ for an object with high neutron transmission. In this case it is anticipated that non-regularized restoration of images without sharp features such as strong edges, which in the spatial frequency domain is

$$\tilde{F}(u,v) = H(u,v)/G(u,v) \tag{6}$$

will yield reasonable results for the restored image $\tilde{F}$. In general, Fourier based methods to do not restore sharp jumps in images in part because of ringing artifacts at these boundaries. Rather more robust restoration methods should be used, such as iterative penalized likelihood restoration algorithms with appropriate penalty functions like the Huber penalty function. Sotthivirat and Fessler have applied such a technique to optical images, [8] and future work will investigate the application to neutron images.

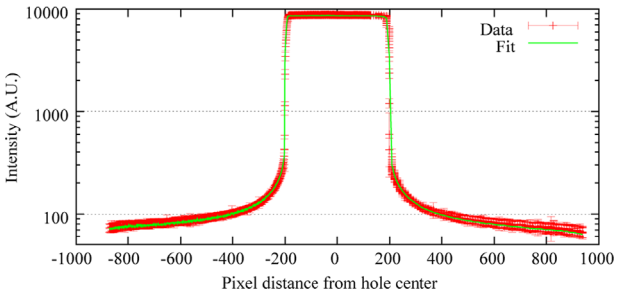

Fig. 3. Line scan through the center of the observed and predicted images of the 5 cm diameter hole for the best fit of the model PSF in Eq. (5) for the amorphous silicon detector.

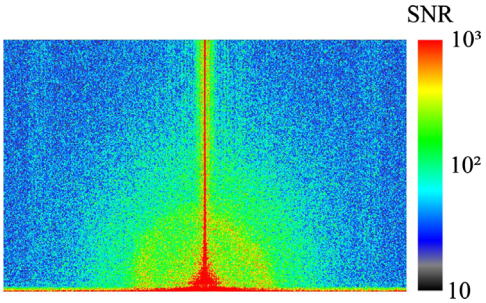

Fig. 4. Ratio of the power spectra of the signal to noise for half the frequency (u,v) plane for the full field of view aluminum step image. Blue corresponds to a SNR of 10, red to a SNR of 1000. Because of this reasonable high SNR and smooth features, it is anticipated that unconstrained image restoration will yield reasonable results. (For interpretation of the references to color in this figure legend, the reader is referred to the web version of this article.)

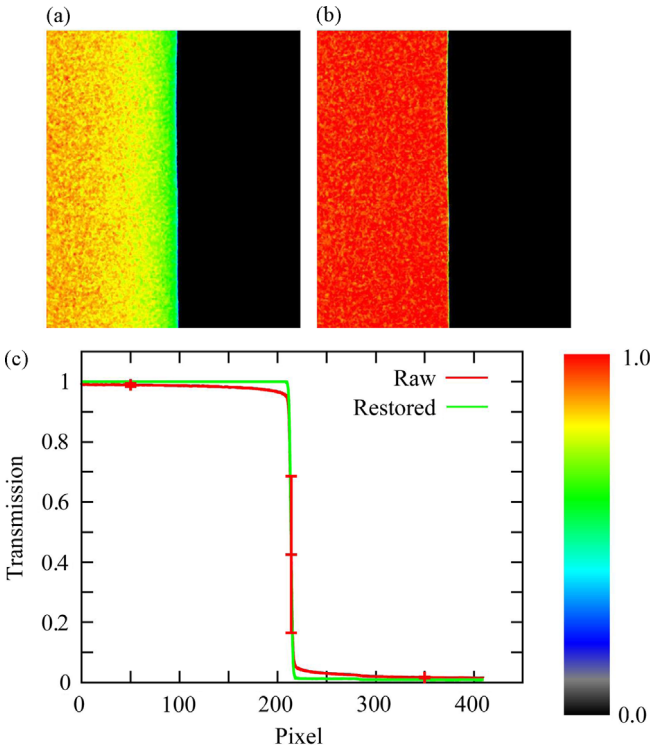

Fig. 5. Colorized and flat-field normalized amorphous silicon images of a Cd edge for (a) no correction, (b) both flat field and edge images restored to correct for the detector PSF. (c) Line profile through the edge for both cases, with error bars that are +/− one standard deviation across the edge drawn at representative locations.

As a first example, the neutron images of a 1 mm thick cadmium sheet are analyzed and restored. The thermal neutron scattering cross-section from cadmium is about 500 times smaller than the thermal neutron absorption cross-section; thus there is no scattered neutron beam to consider. Shown in Fig. 5a is the image of a Cd edge normalized to the flat field. At a distance of over 100 pixels (1.27 cm) the relative intensity has not reached unity. After the Fourier based restoration has been applied to both the flat field and the image edge according to Eq. (5), the transition region is much smaller, and the relative intensity rapidly approaches unity in the open region of the image as shown in Fig. 5b and in the line profiles in Fig. 5c the image of a Cd edge was restored. In this case, both the flat field image and the image of the edge were deconvolved according to Eq. (5) and are shown in comparison with the raw data in Fig. 5b–c. The edge is now much more sharply defined and the neutron transmission probability rapidly approaches unity on the open side of the edge, and zero under the cadmium.

As a second example of restoration, the image of a small section of borated-aluminum is shown Fig. 6. The manufacturer estimated that the amount of boron in this sample should yield a thermal neutron optical density of about 3.2. From the raw images with no restoration, the average optical density observed was 2.7 ± 0.1, which is a 20% discrepancy. The flat field image and sample image were both restored using Eq. (5), and the optical density after restoration was 3.1 ± 0.1, in agreement with the manufacturer's expectation. In addition, it is observed that the edges of the restored image are visually sharper than in the raw, and the overall attenuation in the restored image is on average 20% larger than for the uncorrected images. The restoration therefore yields a better estimate for the attenuation of the object.

As a final example, we apply the correction algorithm to images of a stepped wedge of aluminum. Shown in Fig. 7 are neutron images of the aluminum steps with two different fields of view. The cuvette is an aluminum block, 2.5 cm thick along the beam path, with steps about 3.2 mm wide milled to a maximum depth of 2 cm. The cuvette is located about 5 cm from the scintillator. The beam mask is composed of 1 mm thick lithiated plastic backed by 1.5 mm thick borated aluminum, located about 60 cm from the detector face. Since aluminum is very transparent to neutrons, there should be a negligible scattered neutron beam in these images. More importantly, in both images the scattered beam should be comparable. However, as Fig. 8 shows, there is a large variation when comparing the uncorrected masked to full field of view images: the steps are visible as an intensity gradient from left to right, the outline of the block is clearly visible from the open beam, the screws that secure the lid are visible as well as the stud used for mounting the cuvette. After applying the non-regularized restoration in Eq. (5), the same ratio shows that the variation is less than the random noise, with an order of magnitude reduction in the difference between the two images as compared to the uncorrected case. The only features visible in Fig. 8b are the screws. This may indicate that: a small shift in the optical axis has occurred between image sets; [9] the empirical PSF may be inadequate; the functional form may be incorrect; the detector may not have a uniform PSF; the non-uniform sensitivity of the detector may need to be included in the restoration; there may be noise characteristics that are not fully understood.

4. Conclusions

We have shown that the neutron imaging detector point spread function introduces an effective additive background that is not accounted for in usual neutron image processing, such as flat field normalization. The size of the background increases with the neutron illuminated field of view. If the system point spread

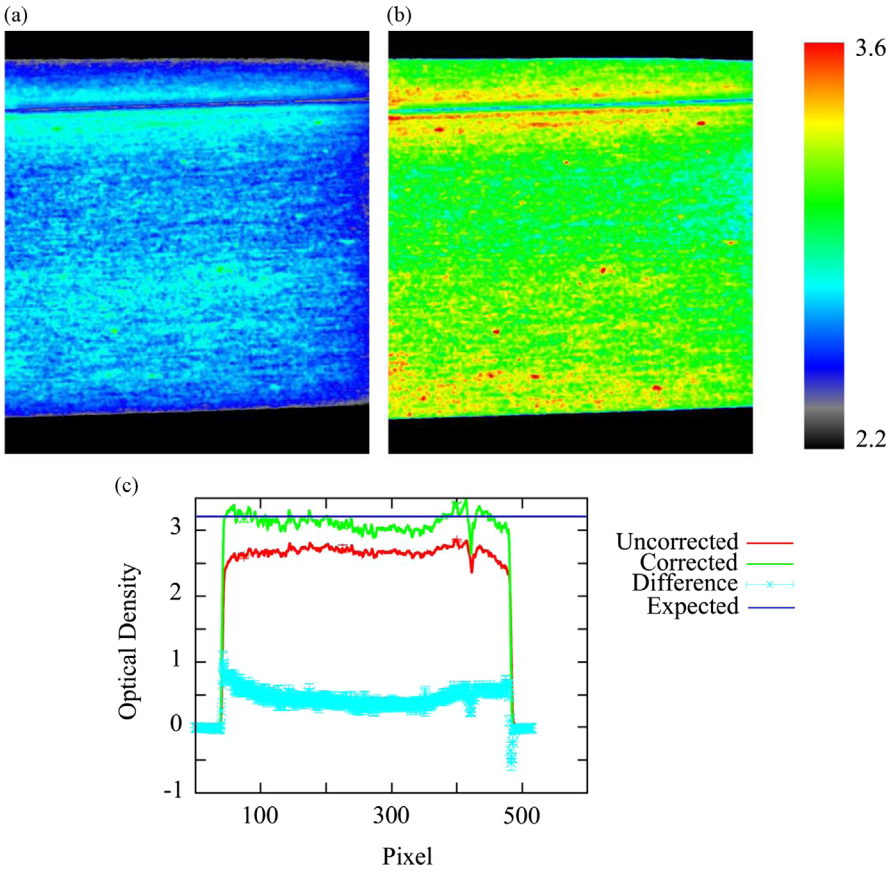

Fig. 6. Comparison of inferred neutron attenuation from raw (a) and restored (b) images of a borated-aluminum coupon. The contrast of each image is set such that black (white) corresponds to an estimated neutron optical density of 2.3 (3.7). (c) A line profile through the center of each image, as well as the difference between the restored and raw optical density images. The expected average optical density was 3.2.

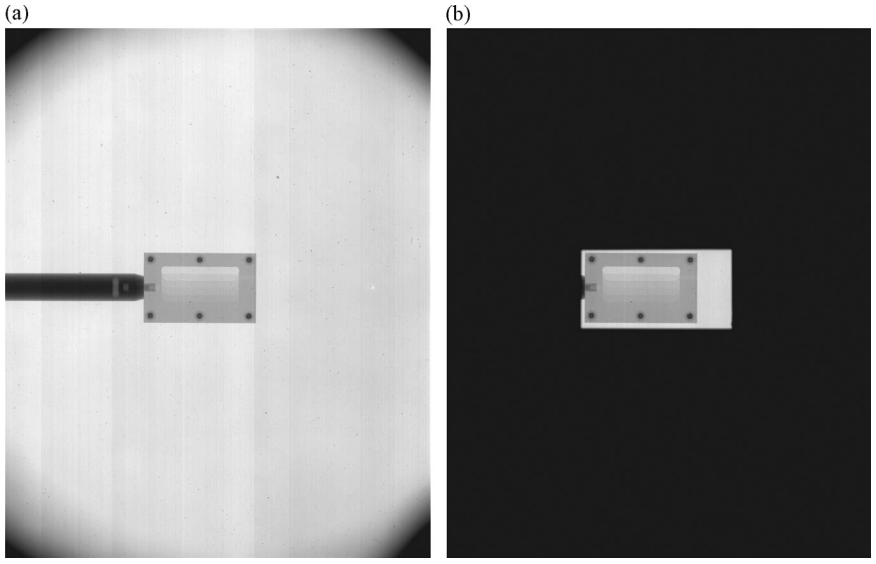

Fig. 7. Neutron images of the aluminum stepped wedge with (a) a full field of view and (b) a masked field of view.

function is properly determined, and image data sets have a high SNR and smooth features, it is possible to use non-regularized restoration in the frequency domain to correct for the detector point spread function, thereby obtaining more accurate estimates of the neutron attenuation which have less or no dependence on the illuminated field of view. This effect is not related to neutron scattering from the sample, but rather the emission of the scintillation light and is thus a source of uncertainty for all neutron imaging methods, including tomography. It is therefore necessary to develop image restoration methods that are appropriate to each

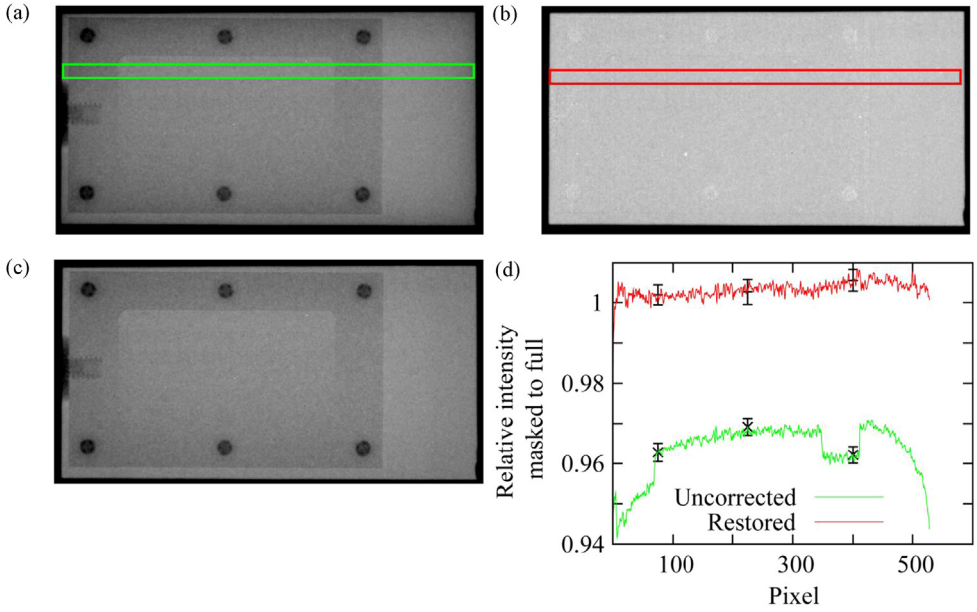

Fig. 8. Comparison of images of the Al steps, normalizing the masked image by the full field of view image (a) uncorrected, (b) restored with Eq. (5) using the PSF in Eq. (4), and (c) restored with Eq. (5) using a truncated version of the PSF in Eq. (4), with $g(r>50)=0$, r in pixels. The truncated restoration clearly does not fully correct the image. (d) A vertical line profile averaging along the box drawn in (a) and (b) shows that the simple restoration reduces the error by more than one order of magnitude. So as to maintain the clarity of the plot, error bars are shown only at representative locations.

detector system in terms of the point spread function and noise characteristics.

Acknowledgments

This work was supported by the U.S. Department of Commerce, the NIST Radiation and Biomolecular Physics Division, the Director's office of NIST, the NIST Center for Neutron Research, and the Department of Energy interagency agreement No. DE_AI01-01EE50660.

References

[1] D.S. Hussey, D.L. Jacobson, M. Arif, K.J. Coakley, D.F. Vecchia, Journal of Fuel Cell Science and Technology **7** (2) (2010).

[2] D.S. Hussey, D.L. Jacobson, in: U. Pasaogullari, C.-Y. Wang (Eds.), Modern Aspects of Electrochemistry, vol. 49, Springer, New York, NY, USA, 2010, pp. 175–199.

[3] R. Hassanein, F. de Beer, N. Kardjilov, E. Lehmann, Physica B-Condensed Matter 385–86 (2006) 1194.

[4] R.S. Fu, J.S. Preston, U. Pasaogullari, T. Shiomi, S. Miyazaki, Y. Tabuchi., D. S. Hussey, D.L. Jacobson, Journal of the Electrochemical Society (2010).

[5] D. Kramer, J.B. Zhang, R. Shimoi, E. Lehmann, A. Wokaun, K. Shinohara, G. G. Scherer, Electrochimica Acta 50 (13) (2005) 2603.

[6] K.R. Castleman, Digital Image Processing, Prentice-Hall, 1996.

[7] D.S. Hussey, D. Spernjak, A.Z. Weber, R. Mukundan, J. Fairweather, E.L. Brosha, J. Davey, J.S. Spendelow, D.L. Jacobson, R.L. Borup, Journal of Applied Physics, 112 (10) (2012) 104906.

[8] S. Sotthivirat, J.A. Fessler, Journal of the Optical Society of America a-Optics Image Science and Vision 20 (3) (2003) 439.

[9] D.S. Hussey, E. Baltic, D.L. Jacobson, Nuclear Instruments and Methods in Physics Research Section A: Accelerators, Spectrometers, Detectors and Associated Equipment (2011).